

# A Fully Printed Flexible MoS<sub>2</sub> Memristive Artificial Synapse with Femtojoule Switching Energy

Xuwei Feng, Yida Li, Lin Wang, Shuai Chen, Zhi Gen Yu, Wee Chong Tan, Nasiruddin Macadam, Guohua Hu, Li Huang, Li Chen, Xiao Gong, Dongzhi Chi, Tawfique Hasan,\* Aaron Voon-Yew Thean,\* Yong-Wei Zhang,\* and Kah-Wee Ang\*

Realization of memristors capable of storing and processing data on flexible substrates is a key enabling technology toward “system-on-plastics”. Recent advancements in printing techniques show enormous potential to overcome the major challenges of the current manufacturing processes that require high temperature and planar topography, which may radically change the system integration approach on flexible substrates. However, fully printed memristors are yet to be successfully demonstrated due to the lack of a robust printable switching medium and a reliable printing process. An aerosol-jet-printed Ag/MoS<sub>2</sub>/Ag memristor is realized in a cross-bar structure by developing a scalable and low temperature printing technique utilizing a functional molybdenum disulfide (MoS<sub>2</sub>) ink platform. The fully printed devices exhibit an ultra-low switching voltage (0.18 V), a high switching ratio (10<sup>7</sup>), a wide range of tuneable resistance states (10–10<sup>10</sup> Ω) for multi-bit data storage, and a low standby power consumption of 1 fW and a switching energy of 4.5 fJ per transition set. Moreover, the MoS<sub>2</sub> memristor exhibits both volatile and non-volatile resistive switching behavior by controlling the current compliance levels, which efficiently mimic the short-term and long-term plasticity of biological synapses, demonstrating its potential to enable energy-efficient artificial neuromorphic computing.

and intelligent applications including personalized feedback therapy, fast speech, and visual recognition.<sup>[1–5]</sup> In particular in the non-conventional space of smart applications requiring conformal attachment on non-flat surfaces such as on-body wearables, the notion of system on plastics (SOP) incorporating neuromorphic computing provides a potential solution.<sup>[1,2]</sup> To build such a flexible neuromorphic system, the fabrication of memristors equipped with synaptic functions is a key step to forming the artificial neural network.<sup>[3–21]</sup> However, current memristor manufacturing technologies such as chemical vapor deposition (CVD),<sup>[7,8,11–13]</sup> spin-coating,<sup>[14,15]</sup> or entire transfer<sup>[16]</sup> impose enormous challenges on flexible substrates as they suffer from high temperature, low yield and complex sacrificial layer removal. Efforts in finding low temperature fabrication technique and robust resistive switching (RS) material are essential to equip the SOP with the data storage and processing capability demanded by target applications.


## 1. Introduction

Neuromorphic computing shows great potential beyond the traditional von Neumann architecture to enable a myriad of innovative

The printing technique—a forefront 3D monolithic integration approach—is suitable for high-volume, low-temperature manufacturing on non-conformal surfaces.<sup>[22–28]</sup> The printing technique is shown to offer more freedom in the design of

X. Feng, Dr. Y. Li, Dr. L. Wang, Dr. W. C. Tan, L. Huang, L. Chen, Prof. X. Gong, Prof. A. V.-Y. Thean, Prof. K.-W. Ang  
Department of Electrical and Computer Engineering  
National University of Singapore  
4 Engineering Drive 3, Singapore 117583  
E-mail: aaron.thean@nus.edu.sg; eleakw@nus.edu.sg

X. Feng, Dr. Y. Li, Dr. L. Wang, Dr. W. C. Tan, L. Huang, L. Chen, Prof. X. Gong, Prof. A. V.-Y. Thean, Prof. K.-W. Ang  
Centre for Advanced 2D Materials  
National University of Singapore  
6 Science Drive 2, Singapore 117546

 The ORCID identification number(s) for the author(s) of this article can be found under <https://doi.org/10.1002/aelm.201900740>.

© 2019 The Authors. Published by WILEY-VCH Verlag GmbH & Co. KGaA, Weinheim. This is an open access article under the terms of the Creative Commons Attribution License, which permits use, distribution and reproduction in any medium, provided the original work is properly cited.

Dr. S. Chen, Dr. Z. G. Yu, Prof. Y.-W. Zhang  
Institute of High Performance Computing  
A\*STAR, 1 Fusionopolis Way, Singapore 138632  
E-mail: zhangyw@ihpc.a-star.edu.sg

N. Macadam, Dr. G. Hu, Dr. T. Hasan  
Cambridge Graphene Centre  
University of Cambridge  
9 JJ Thomson Avenue, Cambridge CB3 0FA, UK  
E-mail: th270@cam.ac.uk

Dr. D. Chi  
Institute of Materials Research and Engineering  
A\*STAR, 2 Fusionopolis Way, Singapore 138634

DOI: 10.1002/aelm.201900740

device geometry and the fabrication of heterostructures. It shows advantages beyond simple solution processed techniques such as spin coating, particularly for large scale fabrication.<sup>[22–28]</sup> However, studies on printable RS media are lacking. Among the conventional RS media, including transition metal oxides (TMOs, e.g., HfO<sub>2</sub>, Al<sub>2</sub>O<sub>3</sub>, TiO<sub>2</sub>),<sup>[4,9,10,16]</sup> polymers,<sup>[15]</sup> and two-dimensional materials (2DMs),<sup>[7,8,11–14,17–21]</sup> the latter shows great potential to realize printed memristors with their solution processability and inherent flexibility. Most printed 2DM demonstration shows robust flexibility.<sup>[22–29]</sup> However, the presence of defect density/vacancies in solution exfoliated 2DM crystals is found to compromise the electrical performance.<sup>[23,27]</sup>

On the other hand, the defects such as sulfur S vacancies in MoS<sub>2</sub> introduced during ultrasonic assisted liquid phase exfoliation (UALPE), play a key role in realizing successful RS by allowing metal ion penetration to form the conductive filaments,<sup>[7,9]</sup> analogous to those observed in biological synapses such as Ca<sup>2+</sup> influx to initialize plasticity.<sup>[9,30,31]</sup> In recent years, molybdenum disulfide (MoS<sub>2</sub>) has emerged as a high-performance RS material<sup>[8,11–14,17–21]</sup> with high switching speed (<15 ns),<sup>[13]</sup> multiple gate-tuneable resistive states,<sup>[8,11,12]</sup> and mechanical flexibility (1200 bending cycles).<sup>[17]</sup> These unique features make printed MoS<sub>2</sub> memristors a natural choice for artificial synapses. In 2017, McManus et al. demonstrated printed read-only memory by shorting the top/bottom electrodes to make logic “1” while introducing printed WS<sub>2</sub> between the two electrodes to suppress the current to make logic “0”.<sup>[22]</sup> However, thus far fully printed memristors with multiple resistive state programmable capabilities and the synaptic functions have not been reported.

Here, we demonstrate a fully aerosol-jet-printed Ag/MoS<sub>2</sub>/Ag vertical memristor in a cross-bar structure on flexible polyimide (PI) substrate by developing a low temperature aerosol-jet printing technique. The vertical structure is printed by alternating the Ag ink and as-formulated MoS<sub>2</sub> ink on different layers. The in-house formulated MoS<sub>2</sub> ink composed of UALPE produced MoS<sub>2</sub> and a binary solvent carrier of isopropyl alcohol (IPA) and 2-butanol, which allows stable jetting and rapid ink drying. The RS mechanism is modeled to be driven by Ag metallic ion diffusion along the vertical and lateral gaps of the printed MoS<sub>2</sub> flakes, allowing fast percolation and formation of conductive filaments. A wide resistance range (10–10<sup>10</sup> Ω) can be easily programmed at different current compliance (CC) which is essential to improve the adaptive learning ability of neuromorphic computing. At a CC level of 200 μA, the fully printed MoS<sub>2</sub> memristor shows forming-free and non-volatile switching characteristics. The switching voltage is ultra low at 0.18 V with a high switching ratio of 10<sup>7</sup>. In addition, an ultra-low standby power consumption of 1 fW and an energy consumption of 4.5 fJ per transition set are achieved, demonstrating its potential use in energy-efficient neuromorphic computing. With the conductance change representing the synaptic weight, the printed MoS<sub>2</sub> memristor successfully emulate a variety of synaptic functions such as the paired-pulse facilitation (PPF), long-term potentiation (LTP) and long-term depression (LTD).

## 2. Results and Discussion

### 2.1. Aerosol-Jet Printing and MoS<sub>2</sub> Ink Formulation

Figure 1a shows the working principles of aerosol-jet printing, which utilizes ultrasonic atomization to generate active ink droplets that are then carried by N<sub>2</sub> gas onto the substrate surface during printing, enabling maskless patterning of materials with fine features. Details of the printing parameters are described in Section 4. Our in-house formulated binder-free MoS<sub>2</sub> ink is composed of ultrasonic assisted liquid phase exfoliated (UALPE) MoS<sub>2</sub> in a binary solvent carrier of 9:1 vol% IPA and 2-butanol. The UALPE employs pure shear forces to allow exfoliation of MoS<sub>2</sub> flakes from the bulk in large quantities at a low setup and production cost.<sup>[28]</sup> Figure 1b shows a photograph of the formulated MoS<sub>2</sub> ink, with a concentration of 0.5 mg mL<sup>-1</sup>. To formulate the ink, a dispersion of MoS<sub>2</sub> flakes is first prepared by UALPE of MoS<sub>2</sub> crystals in *N*-methyl-2-pyrrolidone (NMP). The dispersion is then centrifuged to remove the unexfoliated crystals. Considering the high boiling point of NMP (≈204 °C), it is not suitable for reliable low temperature, uniform deposition of the MoS<sub>2</sub> flakes onto low energy PI substrate. We therefore use a solvent exchange process (high speed centrifugation, followed by redispersion of the supernatant by mild sonication) to formulate a stable ink in IPA and 2-butanol mixture. Previously reported binder-based ink strategy may require an additional processing step (e.g., photonic<sup>[32]</sup> or >200 °C annealing<sup>[24]</sup>) to remove the polymeric binders after printing or water-based inks that may also require high temperature (≈300 °C) post-print annealing to remove residual moisture.<sup>[22]</sup> In contrast, our formulated MoS<sub>2</sub> ink dries rapidly at room temperature (≈150 ms for 40–50 pL individual droplets) without requiring post-deposition processing and enables a uniform deposition through Marangoni enhanced spreading due to the composition of the ink carrier.<sup>[27]</sup> Figure 1c shows an example of aerosol-jet printed pattern onto flexible PI substrate over a 10.0 cm × 11.5 cm area, demonstrating high spatial uniformity for large-scale and complex manufacturing with no loss of printing resolution. Tables S1 and S2, Supporting Information, summarize the formulation method of a variety of MoS<sub>2</sub> inks and the corresponding applications (Section S1, Supporting Information). The optical image in Figure 1d shows multiple printing passes of MoS<sub>2</sub>. The Raman spectra of the deposited MoS<sub>2</sub> show E<sub>2g</sub> at 382.59 cm<sup>-1</sup> and A<sub>1g</sub> at 407.38 cm<sup>-1</sup>, indicating the crystalline nature of the exfoliated flakes from the bulk crystals<sup>[33]</sup> (Figure 1e). The scanning electron microscope (SEM) image in Figure 1f shows that the lateral size of the exfoliated MoS<sub>2</sub> flakes is ≈5–10 μm. The ultrasonic atomization process of aerosol-jet printer further breaks down the MoS<sub>2</sub> flakes into smaller flakes of ≈100–300 nm lateral dimensions. The AFM image in Figure 1g indicates that 10 printing passes ensure sufficient overlap between the deposited flakes to prevent the formation of pin-holes that could result in a short-circuit between the electrodes.

### 2.2. Fully Printed MoS<sub>2</sub> Memristor Architecture

Figure 2a illustrates the schematic of a two-terminal vertical crossbar structure and the photograph of a fully printed

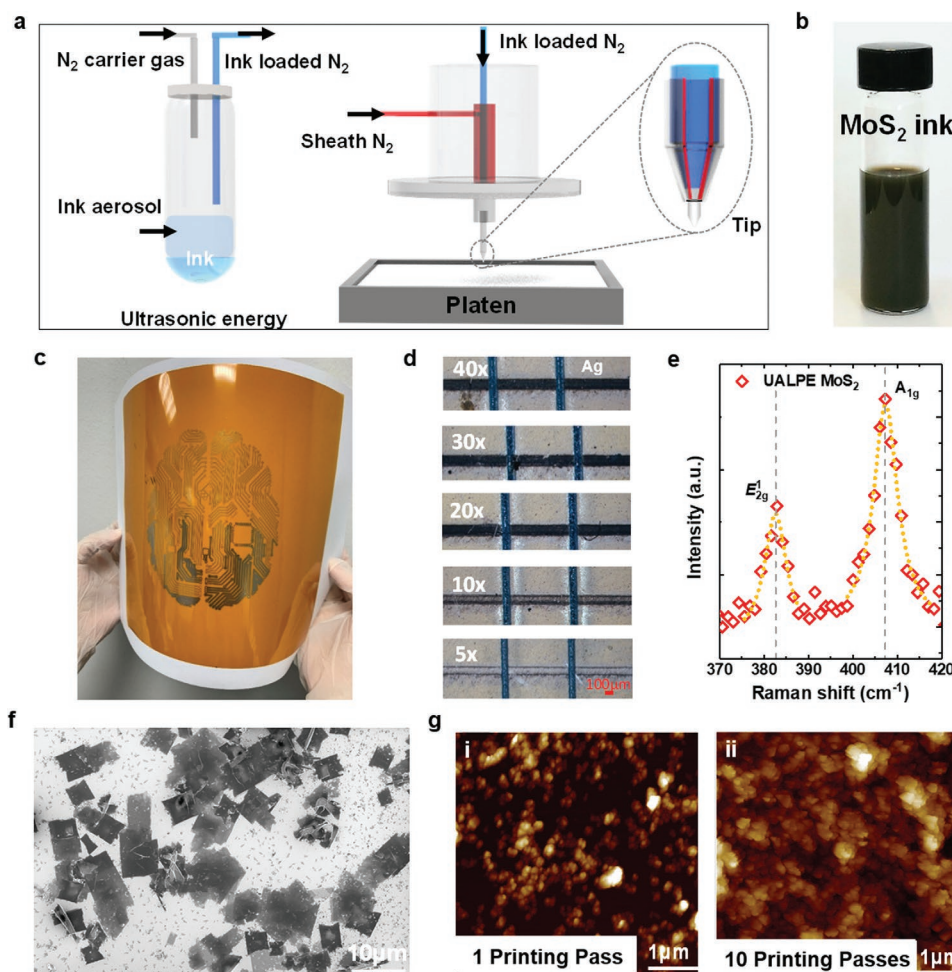


**Figure 1.** Aerosol-jet printing and MoS<sub>2</sub> ink characteristics. a) Schematic plot showing the principles of aerosol jet printing. b) Photograph of the as-formulated MoS<sub>2</sub> functional ink. c) A brain design printed with Ag ink on flexible PI substrate. d) Printed Ag lines (blue) and MoS<sub>2</sub> lines (black) with 5, 10, 20, 30, 40 printing passes, and e) Raman spectrum of the printed MoS<sub>2</sub> collected at an excitation wavelength of 532 nm. The vertical dashed lines indicate the peak positions obtained from Lorentzian fitting of the printed MoS<sub>2</sub> peaks (dotted orange lines), showing the differences in peak positions of 24.79 cm<sup>-1</sup>. f) Top-view scanning electron microscopy (SEM) image of dispersed MoS<sub>2</sub> flakes. g) Atomic force microscopy (AFM) image of printed MoS<sub>2</sub> flakes with i) one and ii) 10 printing passes.

4 × 4 crossbar MoS<sub>2</sub> memristor array on PI. The MoS<sub>2</sub> is printed as the resistive switching medium at the intersections between orthogonal rows and columns of silver (Ag) electrodes, in which they serve as the “bit” lines and “word” lines, respectively. It is worth noting that no complicated substrate treatment such as high temperature curing is required, and all printing processes are carried out in ambient condition. The cross-sectional high-resolution transmission electron microscopy (HR-TEM) image in the left panel of Figure 2b shows the printed memristor architecture in which the MoS<sub>2</sub> is sandwiched between the top and bottom Ag electrodes. The MoS<sub>2</sub> crystal structure is clearly identifiable in the zoomed-in image of the MoS<sub>2</sub> (the right panel of Figure 2b) wherein the structural stability of the layered materials could provide improvements in the robustness of the printed device. The image shows the existence of grain boundaries, which implies the polycrystalline nature of the printed MoS<sub>2</sub> flakes. The energy-dispersive X-ray spectrometry (EDX) elemental map in Figure 2c further confirms the presence and uniform

distribution of Ag, Mo, and S elements. Notably, no oxide signal is detected inside the printed switching layers, which indicates that both the ink formulation and printing are oxidation-free processes. The surface properties of the printed MoS<sub>2</sub> thin films are investigated by X-ray photoelectron spectroscopy (XPS) as shown in Figure 2d. The binding energy of the most intense Mo 3d and S 2p spin-orbit split doublet can be assigned to 228.74 eV (Mo<sup>4+</sup> 3d<sub>5/2</sub>) and 161.53 eV (S<sup>2-</sup> 2p<sub>3/2</sub>), consistent with previously reported semiconducting MoS<sub>2</sub>.<sup>[34]</sup> The atomic composition ratio for Mo and S is found to be 1:1.71, which implies the existence of sulfur vacancies. Details of the XPS analysis is described in Section 4.

### 2.3. Volatile and Non-Volatile Resistive Switching

To characterize the switching performance, we collect current–voltage (*I*–*V*) switching curves measured at CC levels of 100 nA, 1 μA, and 10 μA, as shown in Figure 3a. All the *I*–*V* curves

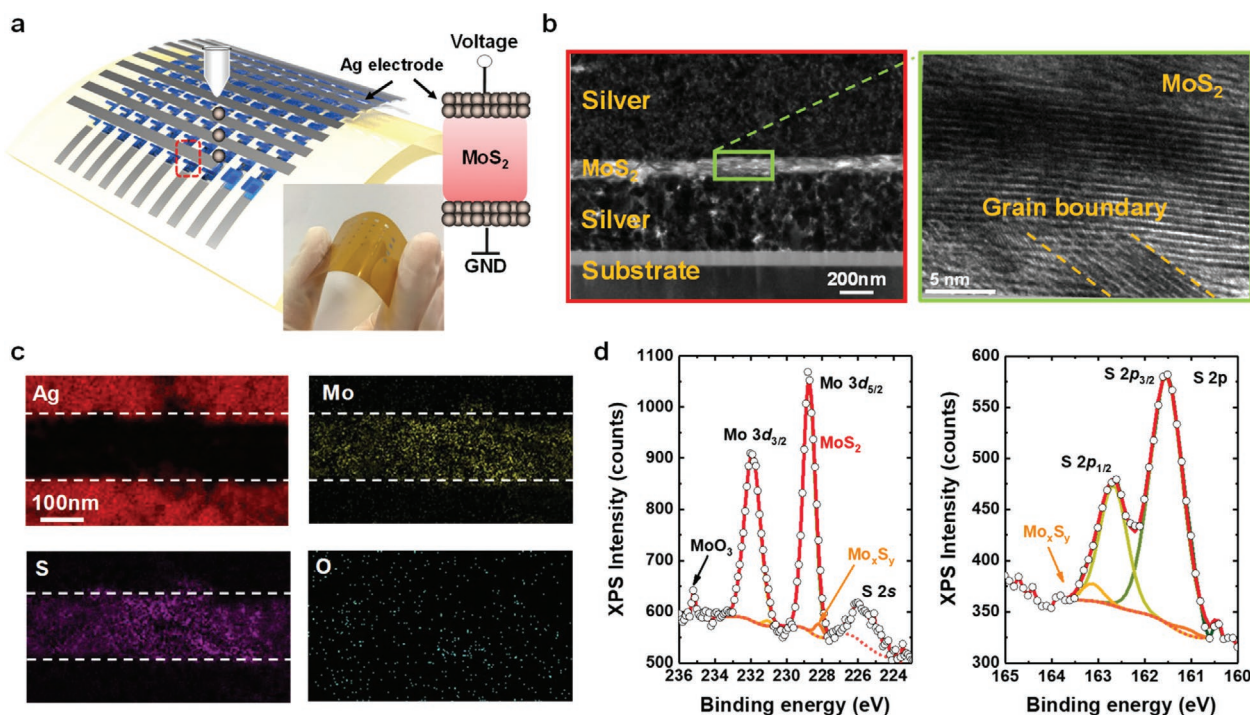


**Figure 2.** Fully printed Ag/MoS<sub>2</sub>/Ag memristor. a) Schematic plot of the fully printed Ag/MoS<sub>2</sub>/Ag memristor in a 4 × 4 cross-bar structure on flexible polyimide substrate. b) Cross-sectional TEM image showing Ag/MoS<sub>2</sub>/Ag vertical stack. The inset shows a zoom-in TEM image of the printed MoS<sub>2</sub> showing its crystalline structure. c) EDX map scan shows a uniform distribution of the Ag, Mo, and S elements. d) XPS spectra of Mo 3d and S 2p signals collected on the printed MoS<sub>2</sub> surface. Core level spectra were collected using a monochromatic Al K $\alpha$  X-ray source ( $h\nu = 1486.69$  eV). The binding energies of all spectra were referenced to C<sub>1s</sub> which is set to 285 eV.

exhibit threshold-type volatile RS behavior, in which the memristor abruptly switches to a low resistance state (LRS) beyond a threshold voltage and then shows resistance recovery when the bias is removed, regardless of the polarity of the sweep voltages. A sharp turn-on slope of  $\approx 5$  mV dec<sup>-1</sup> is observed wherein the super nonlinearity implies its versatility to be used as a two-terminal selector in a 3D stack with memristor to suppress sneak current.<sup>[35]</sup> Subsequently, 100 consecutive  $I$ - $V$  sweeps are performed which indicates the reproducibility of RS and a clear memory window, as shown in Figure 3b. The first sweep highlighted as red indicates the forming-free process. In TMO memristors, a forming-free process is typically required by applying a large voltage to initiate a soft dielectric breakdown and incorporate mobile ions into the insulating film to form a transport channel. Benefiting from the printed defective structure, the first forming voltage is comparable with the subsequent set voltage, which is desirable for practical applications. Interestingly, when a high CC of beyond 100  $\mu$ A is applied, the switching characteristic toggles to a non-volatile behavior, as shown in Figure 3c. In this case, after setting the memristor in LRS with an ultra-low switching voltage of 0.18 V (at CC of 200  $\mu$ A), a voltage bias with opposite polarity is required to reset the memristor to high resistance state (HRS). A high switching ratio of  $10^7$  is achieved at a small reading voltage of 10 mV, the highest reported in flexible memristors so far.<sup>[13,14,16,36–43]</sup> It is noted that a larger CC during the set process might produce a larger and more stable conductive filament, thus a larger reset voltage and reset current is required. Even with the removal of the stress bias, the retention measurement shows that the

LRS is retained for >11 h (Figure 3d). As a result of the low off current of  $\approx 0.1$  pA at a reading voltage of 10 mV as shown in Figure 3d, the standby power is derived as  $P_{\text{standby}} = I_{\text{HRS}} \times V_{\text{read}} = 1$  fW. This effectively suppresses the sneak current and cells disturbance issues. Moreover, multiple resistance states with a wide tuneability range within  $10$ – $10^{10}$   $\Omega$  are also recorded after setting the device to different CC, as shown in Figure 3e, showing great potential for enabling multi-level data storage and multi-state neuromorphic computing.<sup>[10]</sup> Bending tests are also performed to evaluate the mechanical stability of our printed MoS<sub>2</sub> memristor. Despite 1000 bending cycles with testing under different bending radii (down to 5 cm, Section S2, Supporting Information), no degradation in the switching ratio is observed, underscoring the mechanical robustness of the fully printed MoS<sub>2</sub> memristor device.

Figure 3f benchmarks the switching voltage and switching ratio of the fully printed MoS<sub>2</sub> memristor with the state-of-the-art flexible memristors. The printed memristor shows superior performance over its flexible memristor counterparts with a set voltage above 1 V<sup>[13,16,36,37,39–43]</sup> and deficient switching ratio of less than  $10^3$ .<sup>[16,39–43]</sup> Apparently, the 2DMs<sup>[13,14,36–38]</sup> (Region I) demonstrated competitive advantages over the conventional brittle transition metal oxide (TMO)<sup>[16,39–41]</sup> (e.g., NiO<sub>x</sub>, TiO<sub>x</sub>, Region II) and the organic materials (Region III)<sup>[42,43]</sup> due to their inherent flexibility and superior carrier transport properties. In addition, Figure 3f shows that memristors in a cross-bar structure fabricated by transfer method are usually suffering from unsatisfactory performance as compared with single device realized by mechanical exfoliation or spin coating,

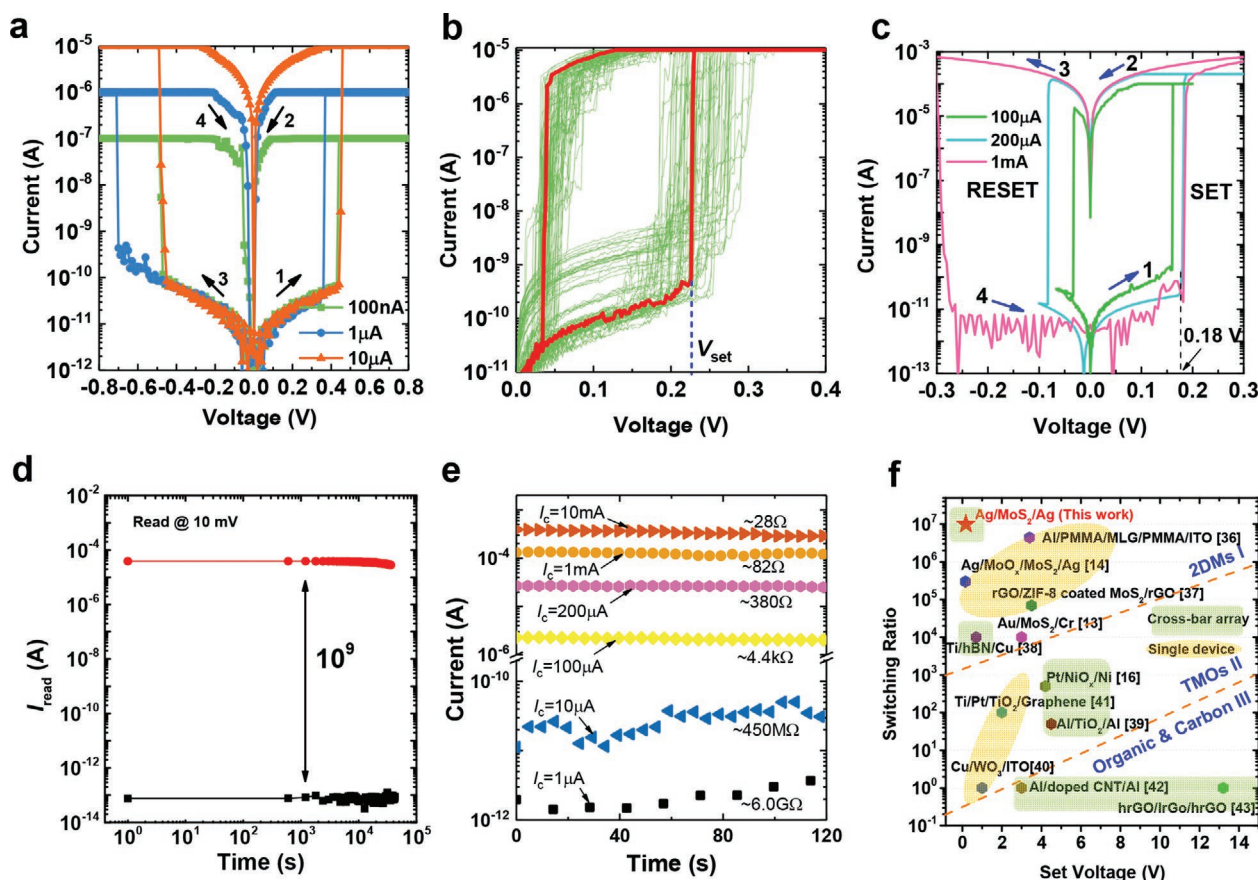


**Figure 3.** Resistive switching characteristics. a) Volatile RS with different CC of 100 nA, 1  $\mu$ A, and 10  $\mu$ A. b)  $I$ - $V$  sweeps of a single device with 100 cycles. An ultra-low set voltage of 0.18–0.3 V is achieved. c) Non-volatile RS with CC of 100  $\mu$ A, 200  $\mu$ A, and 1 mA. d) Data retention at LRS measured by  $I$ - $t$  sampling, collected immediately after setting the device to LRS. The  $V_{read}$  is 10 mV. e) Multiple states of the resistance recorded with varied CC. The read voltage is 10 mV. f) Benchmarking of the fully printed  $MoS_2$  memristor with state-of-the-art memristors fabricated on flexible substrate. It achieves the lowest switching voltage with highest switching ratio.

probably due to the sneak current. The precisely controlled patterning of  $MoS_2$  by printing effectively prevents the cell-to-cell interference and achieves excellent performance in a cross-bar structure. Thus, the aerosol-jet printing technique has significant merits for flexible memristor applications due to the direct top-down fabrication, low-temperature and potential for large scale production. A summary of the figure-of-merit of the flexible memristors is listed in Table S3 (Section S3, Supporting Information). Moreover, using pulse voltage characterization, an ultra-low energy consumption per transition of 4.5 fJ is extracted at a fixed pulse width of 600 ns, which is defined as the switching time of the printed  $MoS_2$  memristor<sup>[18,19]</sup> (Section S4, Supporting Information). The switching voltage (0.18 V), switching ratio ( $10^7$ ), and the power consumption completely meet the International Technology Roadmap for Semiconductors (ITRS) for non-volatile memristor in 2030.<sup>[44,45]</sup>

#### 2.4. Resistive Switching Mechanism

To understand the switching mechanism, conductive atomic force microscope (c-AFM) is used to study the localized switching of the printed  $MoS_2$  layer. The set-up is schematically

shown in Figure 4a. A vertical nano-sized ( $\approx 50$  nm<sup>2</sup>) Pt/printed  $MoS_2/Ag$  structure is constructed as defined by the size of Pt c-AFM tip.<sup>[46]</sup> First, the bottom Ag electrode is grounded, and a ramped voltage stress of 50 mV is applied to the Pt tip across the surface of the printed  $MoS_2$  with one printing pass (Section S5, Supporting Information). The 3D current map plot in Figure 4a confirms the formation of conductive filaments (CFs) with different shapes and sizes.<sup>[7]</sup> With the positive voltage, the S vacancies are expected to play a key role in CFs formation. Subsequently, we performed 50 sequences of  $I$ - $V$  sweeps on the locations where current filaments are detected and found that all of them exhibit volatile RS behavior at a CC of 1  $\mu$ A (Figure 4b), this is consistent with the electrical behavior as shown in Figure 3a. As guided by the arrows, the memristor switches to a LRS (arrow 1) with the applied voltage and subsequently recovers to the HRS (arrow 2) when the voltage is removed. Besides, it is found that faster switching can occur at locations with higher current density (Location 1) while no switching is observed at locations without any current filament (Location 4), as shown in Figure 4c. This confirms that the CFs are easily formed in more defective locations within the  $MoS_2$  switching medium. However, in the practical printed  $MoS_2$  structure with multiple printing passes, the Ag is found

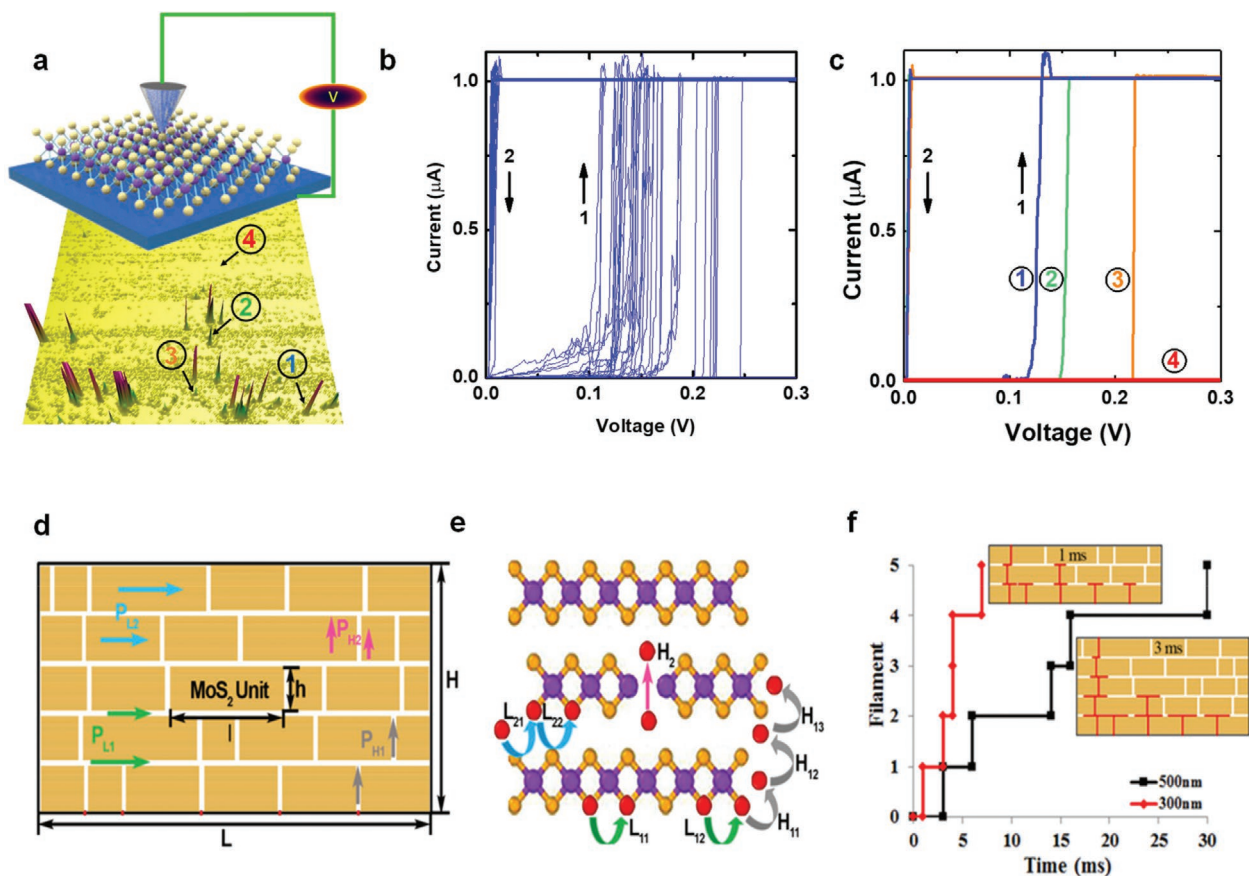


**Figure 4.** Resistive switching mechanism. a) The schematic of the *c*-AFM setting and 3D current map collected on the surface of the printed MoS<sub>2</sub>. b) 50 sequences of *I*-*V* sweeps on the same location of the MoS<sub>2</sub> stack. With a current compliance of 1 μA, volatile switch is observed. Arrow 1 indicates the forward curves and arrow 2 shows the backward curves. c) *I*-*V* sweeps on the four different locations of the MoS<sub>2</sub> stack. Location 1 shows the largest current among the four test areas which achieves the fastest switching. d) kMC and DFT simulations. kMC simulation model with stacked MoS<sub>2</sub> multilayer flakes and possible Ag metallic ions diffusion paths. e) Detailed steps for the possible Ag ions diffusion paths and the corresponding energy barriers. f) Variation of the filament quantity with time for MoS<sub>2</sub> thickness of 300 and 500 nm, respectively.

to play a part in the successful RS. It is found that if the Ag electrode is replaced by printed carbon nanotube (CNT), the RS disappears. Instead, the *I*-*V* curve of CNT/MoS<sub>2</sub>/CNT shows the characteristics of a surface-illuminated photo-detector<sup>[22]</sup> (Section S6, Supporting Information). Considering these two conditions, the switching is most plausibly induced by metal penetration from an active electrode with *S* vacancies exchange.

To further investigate the switching mechanism and the kinetics of Ag filament formation in the printed MoS<sub>2</sub>, a 2D kinetic Monte Carlo (kMC) model is established in Figure 4d. Based on the experimental results, the MoS<sub>2</sub> memristor switching medium layer is likely composed of vertically stacked MoS<sub>2</sub> flakes to form a staggered close-packed structure. In this model, clearly gaps are present between the vertically stacked MoS<sub>2</sub> flakes (bottom-top gap) and the laterally close-packed MoS<sub>2</sub> flakes (side gap). There are two possible horizontal diffusion paths (*P*<sub>L1</sub> and *P*<sub>L2</sub>) and two possible vertical diffusion paths (*P*<sub>H1</sub> and *P*<sub>H2</sub>) for Ag metallic ions to form Ag filaments. *P*<sub>L1</sub> and *P*<sub>L2</sub> are the horizontal diffusion of Ag metallic ions through the bottom-top gaps and through the interlayer space of multilayer MoS<sub>2</sub> flake, respectively. *P*<sub>H1</sub> and *P*<sub>H2</sub> are the vertical diffusion of Ag metallic ions through the side gaps and through the Mo- and S-member ring

within an internal layer of a MoS<sub>2</sub> flake, respectively. Considering all the possible diffusion paths of Ag ions in MoS<sub>2</sub>, we perform density functional theory (DFT) calculations to assess the viability of these paths. Metallic Ag ions are expected to move in the paths with the lowest horizontal and vertical diffusion barriers.<sup>[47]</sup> According to the DFT calculation results, in the horizontal direction, Ag prefers to replace *S* to form an Ag substitutional defect (Ag<sub>S</sub>) and Ag diffusion is mediated by *S* atoms. The calculated energy barriers of the Ag diffusion steps for *L*<sub>11</sub>, *L*<sub>12</sub>, and *L*<sub>22</sub> in Figure 4e are similar, at ≈0.29 eV. However, the energy barrier for Ag ion to diffuse into the MoS<sub>2</sub> interlayer is as high as 1.3 eV (*L*<sub>21</sub> in Figure 4e), which essentially rules out the horizontal diffusion of Ag ions in the interlayer space of multilayer MoS<sub>2</sub> flake. Once Ag ion diffuses to a nearby edge (*H*<sub>11</sub>), it will move to the side gap spontaneously since there is no energy barrier associated with *H*<sub>11</sub>. The energy barrier for Ag ions to diffuse into the side gap (*H*<sub>12</sub>/*H*<sub>13</sub> in Figure 4e) along the vertical direction is 0.31 eV. It should be noted that the energy barrier for Ag ion to diffuse through the Mo- and S-member rings within perfect internal layer of a MoS<sub>2</sub> flake is as high as 8.41 eV and that with one double *S* vacancy is only slightly reduced to 5.78 eV. Therefore, the vertical diffusion of Ag metallic ions through an internal layer

of a MoS<sub>2</sub> flake (H<sub>2</sub> in Figure 4e) is not possible. Hence, the most energetically favorable paths for Ag ions to form Ag filaments are the horizontal diffusion through the bottom-top gaps and vertical diffusion through the side gaps. Based on these paths, we perform kMC simulations with the energy barriers from our DFT calculations. Initially, no Ag ions are present in the printed MoS<sub>2</sub> RRAM switch medium. Subsequently, the Ag ions start to diffuse along both horizontal and vertical directions under the pulse voltage. After 1 ms or 3 ms (the insets in Figure 4f), the first Ag filament is formed when the thickness is 300 or 500 nm. Thereafter, more Ag filaments are formed with increasing simulation time. This may explain the volatile-to-non-volatile transition of the resistive switching behavior of printed MoS<sub>2</sub> memristor. More details of the kMC model and DFT simulation are described in Section S7, Supporting Information. Existing works on MoS<sub>2</sub> switching either relies on migration of oxygen and sulfur ions at

the metal/MoS<sub>2-x</sub>O interface,<sup>[17]</sup> utilizing the metallic phase,<sup>[48]</sup> or the percolation of vacancies through the defects in CVD grown MoS<sub>2</sub>.<sup>[13]</sup> However, the reported switching voltage is considerably higher due to the morphology and defect concentration of the materials. The excess sulfur vacancies induced by UALPE and the unique printed staggered close-packed structure introduce a lot of diffusion pathways for metal ion penetration to form the conductive filaments. Hence, leading to an ultra-low switching voltage and consequently, extremely low power consumption.

## 2.5. Dynamic Response of Artificial Synapse

The printed memristor closely mimics the structure and function of a biological synapse, as shown in Figure 5a, which holds potential to enable neuromorphic computing through

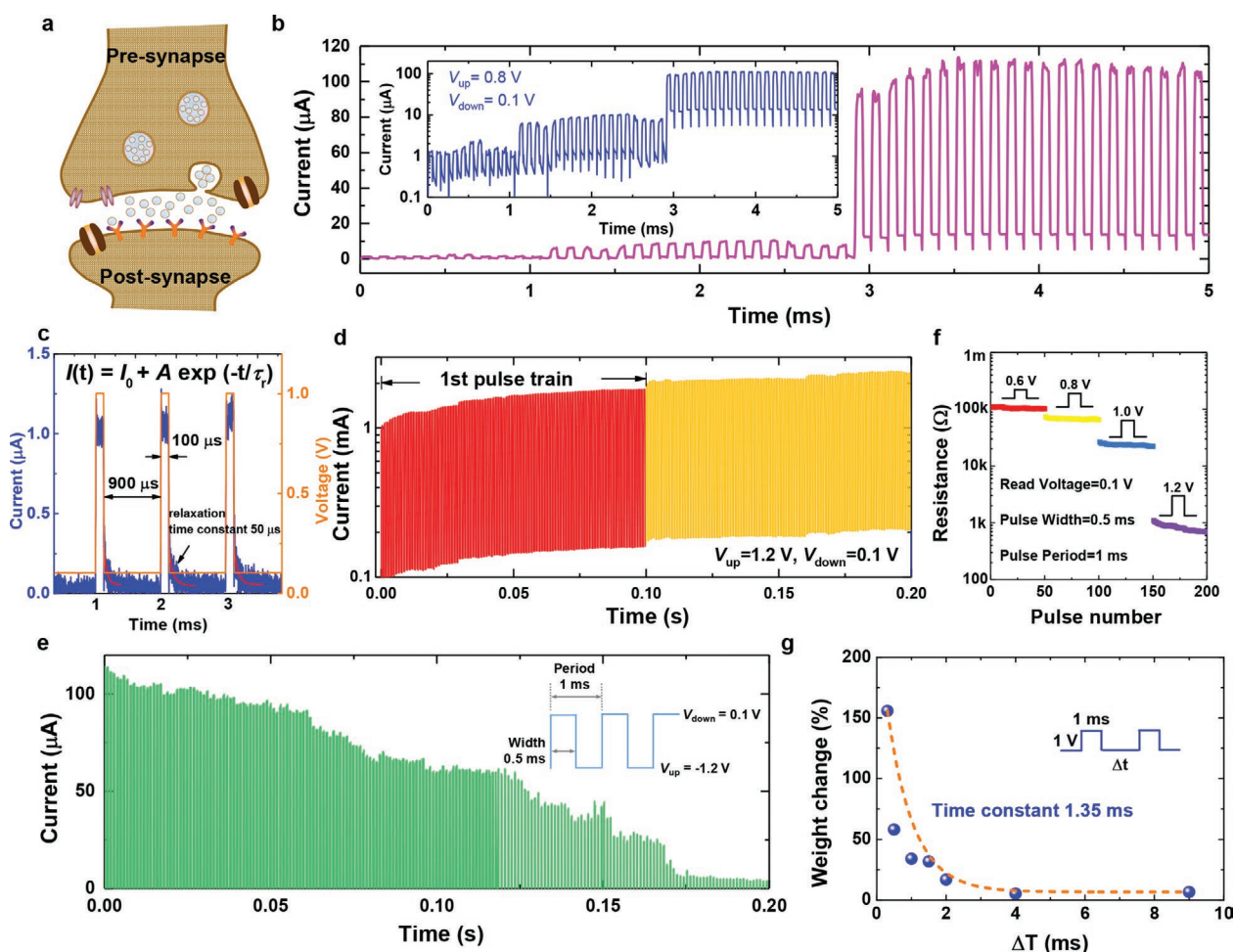


**Figure 5.** Dynamic response of the fully printed MoS<sub>2</sub> memristive artificial synapse. a) Schematic of a biological synaptic junction and the signal transmission between the pre- and post-synaptic neurons. b) Sequence of pulse train showing synapse potentiation. 50  $\mu$ s pulse width and 100  $\mu$ s pulse period were used. Voltage up ( $V_{up}$ , set voltage) is 0.8 V, and voltage down ( $V_{down}$ , read voltage) is 0.1 V. c) Relaxation characteristics with a short pulse width of 100  $\mu$ s and a pulse period of 900  $\mu$ s showing short-term plasticity (STP). Voltage up ( $V_{up}$ , set voltage) is 1 V, and voltage down ( $V_{down}$ , read voltage) is 0.1 V. d) Pulse train with a longer pulse width of 0.5 ms and a larger  $V_{up} = 1.2$  V, showing progressive long-term potentiation (LTP). The read current increases from  $\approx 90$   $\mu$ A to 200  $\mu$ A after 200 pulse train and goes into a stable non-volatile regime. e) Pulse train with  $V_{up} = -1.2$  V, and  $V_{down} = 0.1$  V, showing a progressive long term depression (LTD). f) Post-synaptic resistance versus pulse number at different pulse amplitudes. g) Synaptic weight change versus pulse intervals, which indicates the weight update ability of the printed MoS<sub>2</sub> synapse. The synaptic weight change is the extracted post-synaptic current change corresponding to two successive pulses. The dashed line is an exponential fit with a time constant of 1.35 ms.

synaptic plasticity.<sup>[7,9,30,31]</sup> To study the dynamic response of printed MoS<sub>2</sub> memristor under real working conditions, sequences of pulse train with different amplitude and frequency are applied through the top electrode while simultaneously monitoring the current. In general, the influx processes of pre-synaptic Ca<sup>2+</sup> induce two types of synaptic plasticity, namely short-term and long-term plasticity<sup>[30,31]</sup> that are involved in learning and memory. As shown in Figure 5b, the plasticity of the artificial synapse can be measured by the post-synaptic current (read current  $I_{\text{read}}$ ), which exhibits a progressive increase with the application of a consecutive high-frequency (10 kHz) pre-synaptic pulse train to the memristor. This potentiation process is expected to be related to the growth and clustering of Ag metal ions. At  $t = 3$  ms, the sudden current increase implies the initial formation of conductive path, which is in the same time scale predicted by the kMC model. When a short pulse width of 100  $\mu\text{s}$  is applied, the synapse shows a temporal potentiation and subsequently relaxes due to its volatile nature (Figure 5c). This behavior is analogous to the short-term plasticity in the form of PPF when the biological synapse is subject to a briefer or less intense stimulation.<sup>[30]</sup> The decay during  $\tau_{\text{down}}$  is fitted with an exponential equation,<sup>[49]</sup> showing a relaxation constant of  $\approx 50$   $\mu\text{s}$ . On the other hand, long-term potentiation (LTP) and depression (LTD) are the two forms of activity-dependent long-term synaptic plasticity that last minutes or longer.<sup>[31]</sup> This can be triggered with an intense pulse train to set the synapse into the non-volatile regime. As shown in Figure 5d, the current exhibits a long-lasting increase under positive pulse stimuli with a voltage up ( $V_{\text{up}}$ ) of 1.2 V, voltage down ( $V_{\text{down}}$ ) of 0.1 V, and a frequency of 1 kHz. Since the  $I_{\text{read}}$  goes into non-volatile regime, the current is observed to stay constant when the first pulse train is ended. When the second pulse train is initiated, the current will increase again. This behavior is analogous to LTP. To disrupt the Ag filament and thus relax the synapse, a pulse train with an opposite polarity ( $V_{\text{up}}$  is  $-1.2$  V,  $V_{\text{down}}$  is 0.1 V, and frequency is 1 kHz) is needed to decrease the current, resembling the LTD (Figure 5e). In addition, Figure 5f shows that multiple resistance states can be easily programmed by varying the pulse amplitude, which is found to improve the adaptive learning ability of neuromorphic computing.<sup>[10]</sup> Moreover, Figure 5g depicts that the synaptic weight change can be modulated by the frequency of the applied pulses, where a short time interval between two successive pulses results in a larger potentiation in the memristor weight change. This implies the successful implementation of spike-rate-dependent plasticity (SRDP) characteristic,<sup>[9]</sup> a critical aspect of biological models for neuromorphic computing. The fitted constant of 1.35 ms is comparable to the response time of biological synapses.<sup>[30,31]</sup>

### 3. Conclusion

In conclusion, we have fabricated fully printed, mechanically flexible Ag/MoS<sub>2</sub>/Ag memristors by aerosol-jet printing which demonstrates a robust resistive switching with both volatile and non-volatile memory functions that allow a wide tuneability of discrete resistance states and switching ratios at an ultra-low

switching voltage. In addition, the printed MoS<sub>2</sub> memristors allow a successful emulation of both short- and long-term synaptic plasticity functions including PPF, relaxation, LTP/LTD, and SRDP within one single device, which are promising to enable complex neuromorphic learning. The development of a functional 2D ink platform and a scalable, low temperature printing technology may offer potential to realize large-scale 3D heterogeneous integration on polymeric substrates, which is envisaged to provide a platform to advance printable electronics toward “system-on-plastics.”

### 4. Experimental Section

**Aerosol-Jet Printer:** The entire memristor element was printed using an aerosol-jet printer (Optomec) on Kapton substrates (100  $\mu\text{m}$ ) at room temperature. Ag (Clariant) lines were first deposited with a nozzle diameter of 300  $\mu\text{m}$ . The width of the printed lines was  $\approx 100$   $\mu\text{m}$ , achieved by controlling both the sheath and carrier gas flow. The Ag lines were then transformed into conductive lines via a localized laser sintering process. The MoS<sub>2</sub> switching layer was printed using the ultrasonic mode, where the ink was first sonicated to atomize the ink before being carried out by the N<sub>2</sub> carrier gas. To ensure there was no shorting between the top and bottom Ag electrodes, the MoS<sub>2</sub> medium layer was printed using 10 printing passes.

**Electrical Measurement:**  $I$ - $V$  sweeps were measured in ambient condition at room temperature using an Agilent 4155B semiconductor parameter analyzer and a probe station. The pulse measurements were carried out using a Cascade probe station connecting to a 4200-SCS Keithley semiconductor analyzer. The applied pulse amplitude is larger than the set voltage in  $I$ - $V$  measurement probably due to the parasitic resistance of the equipment.

**XPS:** Core level spectra were collected using a monochromatic Al K $\alpha$  X-ray source ( $h\nu = 1486.69$  eV). The binding energies of all spectra were referenced to C 1s which was set to 285 eV. Then Gaussian and Lorentzian line shapes with a Shirley background subtraction were used to fit the raw data. For the S 2p core level spectra, the well-resolved two peaks corresponding to S 2p<sub>1/2</sub> (162.67 eV) and S 2p<sub>3/2</sub> (161.53 eV) were extracted. For the Mo 3d core level spectra, two core level peaks at 228.74 and 231.91 eV could be attributed to Mo 3d<sub>5</sub> and Mo 3d<sub>3</sub>. Besides, a small amount (3.28%) of molybdenum oxide was also observed at 235.22 eV. The atomic ratio of S/Mo was calculated as the atomic concentration of S over Mo and Mo oxides.

### Supporting Information

Supporting Information is available from the Wiley Online Library or from the author.

### Acknowledgements

This research was supported by A\*STAR Science and Engineering Research Council (Grant Nos 152-70-00013 and 152-70-00017), Singapore National Research Foundation's Returning Singapore Scientist Scheme (Grant No NRF-RSS2015-003), and by the National Research Foundation, Prime Minister's Office, Singapore. N. Macadam would like to acknowledge support from EPSRC (EP/L016087/1).

### Conflict of Interest

The authors declare no conflict of interest.



## Keywords

artificial synapse, ink formulation, memristor, molybdenum disulfide, printing

Received: July 19, 2019  
Revised: August 8, 2019  
Published online:

- [1] D. Son, J. Lee, S. Qiao, R. Ghaffari, J. Kim, J. E. Lee, C. Song, S. J. Kim, D. J. Lee, S. W. Jun, S. Yang, M. Park, J. Shin, K. Do, M. Lee, K. Kang, C. S. Hwang, N. Lu, T. Hyeon, D.-H. Kim, *Nat. Nanotechnol.* **2014**, *9*, 397.
- [2] S. Xu, Y. Zhang, L. Jia, K. E. Mathewson, K.-I. Jang, J. Kim, H. Fu, X. Huang, P. Chava, R. Wang, S. Bhole, L. Wang, Y. J. Na, Y. Guan, M. Flavin, Z. Han, Y. Huang, J. A. Rogers, *Science* **2014**, *344*, 70.
- [3] Q. Xia, J. J. Yang, *Nat. Mater.* **2019**, *18*, 309.
- [4] Z. Wang, S. Joshi, S. Savel'ev, W. Song, R. Midya, Y. Li, M. Rao, P. Yan, S. Asapu, Y. Zhuo, *Nat. Elect.* **2018**, *1*, 137.
- [5] R. Midya, Z. Wang, S. Asapu, S. Joshi, Y. Li, Y. Zhuo, W. Song, H. Jiang, N. Upadhyay, M. Rao, P. Lin, C. Li, Q. Xia, J. J. Yang, *Adv. Electron. Mater.* **2019**, *5*, 1900060.
- [6] D. Ielmini, H.-S. P. Wong, *Nat. Elect.* **2018**, *1*, 333.
- [7] Y. Shi, X. Liang, B. Yuan, V. Chen, H. Li, F. Hui, Z. Yu, F. Yuan, E. Pop, H. S. P. Wong, M. Lanza, *Nat. Elect.* **2018**, *1*, 458.
- [8] V. K. Sangwan, H.-S. Lee, H. Bergeron, I. Balla, M. E. Beck, K.-S. Chen, M. C. Hersam, *Nature* **2018**, *554*, 500.
- [9] Z. Wang, S. Joshi, S. E. Savel'ev, H. Jiang, R. Midya, P. Lin, M. Hu, N. Ge, J. P. Strachan, Z. Li, Q. Wu, M. Barnell, G.-L. Li, H. L. Xin, R. S. Williams, Q. Xia, J. J. Yang, *Nat. Mater.* **2016**, *16*, 101.
- [10] S. Yu, B. Gao, Z. Fang, H. Yu, J. Kang, H.-S. P. Wong, *Adv. Mater.* **2013**, *25*, 1774.
- [11] L. Wang, W. Liao, S. L. Wong, Z. G. Yu, S. Li, Y.-F. Lim, X. Feng, W. C. Tan, X. Huang, L. Chen, L. Liu, J. Chen, X. Gong, C. Zhu, X. Liu, Y.-W. Zhang, D. Chi, K.-W. Ang, *Adv. Funct. Mater.* **2019**, *29*, 1901106.
- [12] V. K. Sangwan, D. Jariwala, I. S. Kim, K.-S. Chen, T. J. Marks, L. J. Lauhon, M. C. Hersam, *Nat. Nanotechnol.* **2015**, *10*, 403.
- [13] R. Ge, X. Wu, M. Kim, J. Shi, S. Sonde, L. Tao, Y. Zhang, J. C. Lee, D. Akinwande, *Nano Lett.* **2018**, *18*, 434.
- [14] A. A. Bessonov, M. N. Kirikova, D. I. Petukhov, M. Allen, T. Ryhänen, M. J. Bailey, *Nat. Mater.* **2015**, *14*, 199.
- [15] S. Goswami, A. J. Matula, S. P. Rath, S. Hedström, S. Saha, M. Annamalai, D. Sengupta, A. Patra, S. Ghosh, H. Jani, *Nat. Mater.* **2017**, *16*, 1216.
- [16] S. Kim, J. H. Son, S. H. Lee, B. K. You, K. I. Park, H. K. Lee, M. Byun, K. J. Lee, *Adv. Mater.* **2014**, *26*, 7480.
- [17] M. Wang, S. Cai, C. Pan, C. Wang, X. Lian, Y. Zhuo, K. Xu, T. Cao, X. Pan, B. Wang, *Nat. Elect.* **2018**, *1*, 130.
- [18] J. Zhu, Y. Yang, R. Jia, Z. Liang, W. Zhu, Z. U. Rehman, L. Bao, X. Zhang, Y. Cai, L. Song, R. Huang, *Adv. Mater.* **2018**, *30*, 1800195.
- [19] R. A. John, F. Liu, N. A. Chien, M. R. Kulkarni, C. Zhu, Q. Fu, A. Basu, Z. Liu, N. Mathews, *Adv. Mater.* **2018**, *30*, 1800220.
- [20] J. Jiang, J. Guo, X. Wan, Y. Yang, H. Xie, D. Niu, J. Yang, J. He, Y. Gao, Q. Wan, *Small* **2017**, *13*, 1700933.
- [21] H.-K. He, R. Yang, W. Zhou, H.-M. Huang, J. Xiong, L. Gan, T.-Y. Zhai, X. Guo, *Small* **2018**, *14*, 1800079.
- [22] D. McManus, S. Vranic, F. Withers, V. Sanchez-Romaguera, M. Macucci, H. Yang, R. Sorrentino, K. Parvez, S.-K. Son, G. Iannaccone, K. Kostarelos, G. Fiori, C. Casiraghi, *Nat. Nanotechnol.* **2017**, *12*, 343.
- [23] A. G. Kelly, T. Hallam, C. Backes, A. Harvey, A. S. Esmaily, I. Godwin, J. Coelho, V. Nicolosi, J. Lauth, A. Kulkarni, *Science* **2017**, *356*, 69.
- [24] J. Li, M. M. Naiini, S. Vaziri, M. C. Lemme, M. Östling, *Adv. Funct. Mater.* **2014**, *24*, 6524.
- [25] J. Kwon, Y. Takeda, R. Shiwaku, S. Tokito, K. Cho, S. Jung, *Nat. Commun.* **2019**, *10*, 54.
- [26] T. Carey, S. Cacovich, G. Divitini, J. Ren, A. Mansouri, J. M. Kim, C. Wang, C. Ducati, R. Sordan, F. Torrisi, *Nat. Commun.* **2017**, *8*, 1202.
- [27] G. Hu, T. Albrow-Owen, X. Jin, A. Ali, Y. Hu, R. C. T. Howe, K. Shehzad, Z. Yang, X. Zhu, R. I. Woodward, T.-C. Wu, H. Jussila, J.-B. Wu, P. Peng, P.-H. Tan, Z. Sun, E. J. R. Kelleher, M. Zhang, Y. Xu, T. Hasan, *Nat. Commun.* **2017**, *8*, 278.
- [28] G. Hu, J. Kang, L. W. T. Ng, X. Zhu, R. C. T. Howe, C. G. Jones, M. C. Hersam, T. Hasan, *Chem. Soc. Rev.* **2018**, *47*, 3265.
- [29] D. Song, A. Mahajan, E. B. Secor, M. C. Hersam, L. F. Francis, C. D. Frisbie, *ACS Nano* **2017**, *11*, 7431.
- [30] W. A. Catterall, A. P. Few, *Neuron* **2008**, *59*, 882.
- [31] S.-N. Yang, Y.-G. Tang, R. S. Zucker, *J. Neurophysiol.* **1999**, *81*, 781.
- [32] E. B. Secor, B. Y. Ahn, T. Z. Gao, J. A. Lewis, M. C. Hersam, *Adv. Mater.* **2015**, *27*, 6683.
- [33] C. Lee, H. Yan, L. E. Brus, T. F. Heinz, J. Hone, S. Ryu, *ACS Nano* **2010**, *4*, 2695.
- [34] P. Xia, X. Feng, R. J. Ng, S. Wang, D. Chi, C. Li, Z. He, X. Liu, K.-W. Ang, *Sci. Rep.* **2017**, *7*, 40669.
- [35] R. Midya, Z. Wang, J. Zhang, S. E. Savel'ev, C. Li, M. Rao, M. H. Jang, S. Joshi, H. Jiang, P. Lin, K. Norris, N. Ge, Q. Wu, M. Barnell, Z. Li, H. L. Xin, R. S. Williams, Q. Xia, J. J. Yang, *Adv. Mater.* **2017**, *29*, 1604457.
- [36] D. I. Son, T. W. Kim, J. H. Shim, J. H. Jung, D. U. Lee, J. M. Lee, W. I. Park, W. K. Choi, *Nano Lett.* **2010**, *10*, 2441.
- [37] X. Huang, B. Zheng, Z. Liu, C. Tan, J. Liu, B. Chen, H. Li, J. Chen, X. Zhang, Z. Fan, W. Zhang, Z. Guo, F. Huo, Y. Yang, L.-H. Xie, W. Huang, H. Zhang, *ACS Nano* **2014**, *8*, 8695.
- [38] C. Pan, Y. Ji, N. Xiao, F. Hui, K. Tang, Y. Guo, X. Xie, F. M. Puglisi, L. Larcher, E. Miranda, *Adv. Funct. Mater.* **2017**, *27*, 1604811.
- [39] S. Kim, H. Y. Jeong, S. K. Kim, S.-Y. Choi, K. J. Lee, *Nano Lett.* **2011**, *11*, 5438.
- [40] Y. Ji, Y. Yang, S.-K. Lee, G. Ruan, T.-W. Kim, H. Fei, S.-H. Lee, D.-Y. Kim, J. Yoon, J. M. Tour, *ACS Nano* **2016**, *10*, 7598.
- [41] M. Qian, Y. Pan, F. Liu, M. Wang, H. Shen, D. He, B. Wang, Y. Shi, F. Miao, X. Wang, *Adv. Mater.* **2014**, *26*, 3275.
- [42] S. K. Hwang, J. M. Lee, S. Kim, J. S. Park, H. I. Park, C. W. Ahn, K. J. Lee, T. Lee, S. O. Kim, *Nano Lett.* **2012**, *12*, 2217.
- [43] J. Liu, Z. Yin, X. Cao, F. Zhao, L. Wang, W. Huang, H. Zhang, *Adv. Mater.* **2013**, *25*, 233.
- [44] F. Hui, E. Grustan-Gutierrez, S. Long, Q. Liu, A. K. Ott, A. C. Ferrari, M. Lanza, *Adv. Electron. Mater.* **2017**, *3*, 1600195.
- [45] M. Lanza, H.-S. P. Wong, E. Pop, D. Ielmini, D. Strukov, B. C. Regan, L. Larcher, M. A. Villena, J. J. Yang, L. Goux, A. Belmonte, Y. Yang, F. M. Puglisi, J. Kang, B. Magyari-Köpe, E. Yalon, A. Kenyon, M. Buckwell, A. Mehonic, A. Shluger, H. Li, T.-H. Hou, B. Hudec, D. Akinwande, R. Ge, S. Ambrogio, J. B. Roldan, E. Miranda, J. Suñe, K. L. Pey, X. Wu, N. Raghavan, E. Wu, W. D. Lu, G. Navarro, W. Zhang, H. Wu, R. Li, A. Holleitner, U. Wurstbauer, M. C. Lemme, M. Liu, S. Long, Q. Liu, H. Lv, A. Padovani, P. Pavan, I. Valov, X. Jing, T. Han, K. Zhu, S. Chen, F. Hui, Y. Shi, *Adv. Electron. Mater.* **2018**, *5*, 1800143.
- [46] W. Frammelsberger, G. Benstetter, J. Kiely, R. Stamp, *Appl. Surf. Sci.* **2007**, *253*, 3615.
- [47] F. Raffone, F. Risplendi, G. Cicero, *Nano Lett.* **2016**, *16*, 2543.
- [48] P. Cheng, K. Sun, Y. H. Hu, *Nano Lett.* **2016**, *16*, 572.
- [49] M.-K. Kim, J.-S. Lee, *ACS Nano* **2018**, *12*, 1680.